

Large transverse thermoelectric figure of merit in a topological Dirac semimetal

JunSen Xiang^{1,2}, SiLe Hu^{1,3}, Meng Lyu^{1,3}, WenLiang Zhu^{1,3}, ChaoYang Ma^{1,3}, ZiYu Chen², Frank Steglich^{1,4}, GenFu Chen^{1,3,5}, and PeiJie Sun^{1,3,5*}

¹ Beijing National Laboratory for Condensed Matter Physics, Institute of Physics, Chinese Academy of Sciences, Beijing 100190, China;

² Department of Physics, Key Laboratory of Micro-Nano Measurement-Manipulation and Physics, Beihang University, Beijing 100191, China;

³ University of Chinese Academy of Sciences, Beijing 100049, China;

⁴ Max Planck Institute for Chemical Physics of Solids, Dresden 01187, Germany;

⁵ Songshan Lake Materials Laboratory, Dongguan 523808, China

Received September 4, 2019; accepted September 11, 2019; published online November 19, 2019

The Seebeck effect encounters a few fundamental constraints hindering its thermoelectric (TE) conversion efficiency. Most notably, there are the charge compensation of electrons and holes that diminishes this effect, and the Wiedemann-Franz (WF) law that makes independent optimization of the corresponding electrical and thermal conductivities impossible. Here, we demonstrate that in the topological Dirac semimetal Cd_3As_2 the Nernst effect, i.e., the transverse counterpart of the Seebeck effect, can generate a large TE figure of merit $z_N T$. At room temperature, $z_N T \approx 0.5$ in a small field of 2 T and it significantly surmounts its longitudinal counterpart for any field. A large Nernst effect is generically expected in topological semimetals, benefiting from both the bipolar transport of compensated electrons and holes and their high mobilities. In this case, heat and charge transport are orthogonal, i.e., not intertwined by the WF law anymore. More importantly, further optimization of $z_N T$ by tuning the Fermi level to the Dirac node can be anticipated due to not only the enhanced bipolar transport, but also the anomalous Nernst effect arising from a pronounced Berry curvature. A combination of the topologically trivial and nontrivial advantages promises to open a new avenue towards high-efficient transverse thermoelectricity.

Dirac semimetal, Cd_3As_2 , Nernst effect, transverse thermoelectricity

PACS number(s): 72.15.Jf, 81.05.Bx, 75.47.-m

Citation: J. S. Xiang, S. L. Hu, M. Lyu, W. L. Zhu, C. Y. Ma, Z. Y. Chen, F. Steglich, G. F. Chen, and P. J. Sun, Large transverse thermoelectric figure of merit in a topological Dirac semimetal, *Sci. China-Phys. Mech. Astron.* **63**, 237011 (2020), <https://doi.org/10.1007/s11433-019-1445-4>

1 Introduction

Thermoelectric (TE) devices can convert heat into electrical energy but may also be used as a heat pump in which electricity can drive a Peltier cooler. Various materials and differing concepts have been employed in order to achieve practical application [1,2]. Here, the dimensionless figure of

merit, $z_S T = TS_{xx}^2 / \rho_{xx} \kappa_{xx}$, plays the key role in characterizing the TE conversion efficiency. It contains the absolute temperature T , the Seebeck coefficient S_{xx} , the electrical resistivity ρ_{xx} and the thermal conductivity κ_{xx} . The subscript “xx”, which denotes diagonal components of the corresponding transport matrix, is intentionally added to distinguish from the off-diagonal counterparts that will define the transverse TE figure of merit $z_N T$. In classical TE materials, optimization of $z_S T$ meets severe limitations. Most important

*Corresponding author (email: pjsun@iphy.ac.cn)

is charge compensation of electrons and holes that contribute oppositely to S_{xx} (Figure 1(a)). Also, the Lorenz number fundamentally ties ρ_{xx} and the electronic contribution to thermal conductivity κ_{xx}^e , i.e., $L = \kappa_{xx}^e \rho_{xx} / T$. L coincides with the Sommerfeld's constant $L_0 = 2.44 \times 10^{-8} \text{ W } \Omega \text{ K}^2$ for dominating elastic scatterings (the WF law). Though the WF law is frequently violated to some extent at finite temperatures, it makes independent optimization of ρ_{xx} and κ_{xx} for high $z_S T$ impossible. Any new designing principle circumventing (some of) these limitations will potentially achieve a big advance in TE application, such as the electron crystal-phonon glass approach, which proposes to minimize κ_{xx} while simultaneously keeping ρ_{xx} low by crystal-structure engineering [3].

A number of suited TE materials have recently been revisited and turned out to be topological materials [2,4]. Except for some basic properties connecting both types of materials [4], e.g., the presence of heavy elements and small band gaps, characteristic reasons for advanced TE transport in topological materials have also been discussed. These include the specific band complexities [5-7] and charge relaxation processes [8-10] generally related to topological materials. However, the aforementioned topologically trivial limitations for TE performance exist for topological materials as well. Another, largely unexplored, prominent feature of these materials is the strong magnetic-field response, pertinent particularly to topological semimetals [11,12]. Here, in addition to the well-known chiral anomaly in the magneto-electrical conductivity, a strong effect of magnetic field on the Seebeck effect was recently realized, too. For example, Wang et al. [13] have reported a largely enhanced $z_S T$ from 0.2 to 1.2 by applying a field $B = 7 \text{ T}$ at $T = 370 \text{ K}$ for Cd_3As_2 . Moreover, a large, nonsaturating Seebeck effect in quantizing magnetic fields has been theoretically predicted for topological Dirac/Weyl semimetals [14].

When a magnetic field B_z is applied orthogonally to the temperature gradient dT_x , a transverse counterpart (S_{xy}) of S_{xx} , known as the Nernst effect (Figure 1(b)), appears too. Traditionally, S_{xy} has been intensively investigated mainly in elemental Bi and several of its binary alloys, like Bi-Sb [15-18], where its potential for TE application was first proposed, as well as in some electron-correlated materials [19]. The key ingredients for significant values of $S_{xy}(B_z)$ revealed in these works include: a large product of $\omega_c \tau$ (ω_c is the cyclotron frequency and τ the relaxation time) and a small Fermi energy ε_F (see Supporting Information for the explanation why S_{xy} tracks $\omega_c \tau / \varepsilon_F$ in a single-band approximation), as well as a strong electron-hole compensation that gives rise to a significant bipolar effect, see Figure 1(b). Interestingly, similar conditions are inherent to a large number of recently discovered topological semimetals [12]. Indeed, a large Nernst power factor, S_{xy}^2 / ρ , was found in NbP [20], where, however, a large thermal conductivity prevents realization of a sizable

transverse figure of merit $z_N T$. Furthermore, an anomalous Nernst effect (ANE) due to a pronounced Berry curvature of the related electronic bands, in addition to the aforementioned topological trivial origins, has been proposed [8,21-27] for topological conducting materials with Dirac/Weyl nodes sufficiently close to ε_F . Experimental verifications of ANE were reported very recently for NbP [26,27], TaP/TaAs [24] and Cd_3As_2 [25].

In this paper, we demonstrate that the topological Dirac semimetal Cd_3As_2 exhibits a sizable transverse figure of merit which surmounts its longitudinal counterpart in a wide temperature range above 100 K, amounting to $z_N T \approx 0.5$ (0.7) at $T = 300$ (350) K in $B_z = 2$ (2.5) T. These $z_N T$ values, after being normalized by the corresponding field, are more than 2 times its longitudinal counterpart $z_S T$ in this temperature window. More importantly, due to the removal of the two constraints that apply inherently to S_{xx} (see Figure 1(b)), as well as the theoretically predicted addition of the ANE, the transverse thermoelectricity in topological semimetals appears to be much easier for further optimization by e.g., tuning the Fermi level.

2 Materials and methods

2.1 Sample synthesis

Single crystals of Cd_3As_2 were grown by self-transport technique. Stoichiometric amounts of cadmium and arsenic were first sealed in an evacuated quartz ampoule. The quartz ampoule was heated to 850°C and then quenched in liquid nitrogen. The obtained polycrystalline Cd_3As_2 was filled in a quartz ampoule again. After evacuating and sealing, the ampoule was placed in a two-zone furnace with a temperature gradient from 575°C to 500°C for 10 days, and then naturally cooled down to room temperature. The single crystals grow in bulk form with well-defined facets, see inset of Figure S1. X-ray diffraction of powdered and single-crystalline samples was performed to confirm the proper crystal structure and the orientation (Figure S1). The residual resistivity ratio $\text{RRR} = \rho_{xx}(300 \text{ K}) / \rho_{xx}(2 \text{ K})$ is between 5 and 10 for all the samples investigated. This is in agreement with most published works on this compound [13,28,29], except for several batches reported in ref. [30].

2.2 Transport measurements

The three relevant thermal transport coefficients S_{xx} , S_{xy} and κ_{xx} , as well as resistivity ρ_{xx} were measured simultaneously and adiabatically in a magnetic field B_z applied orthogonal to temperature gradient dT_x (Figure 1(a), (b) and (c) inset). dT_x was monitored by a field-calibrated, thin Chromel-AuFe0.07% thermocouple ($\varphi = 25 \mu\text{m}$), cf. Figure S2. All the five samples investigated in this work were bar-shaped by

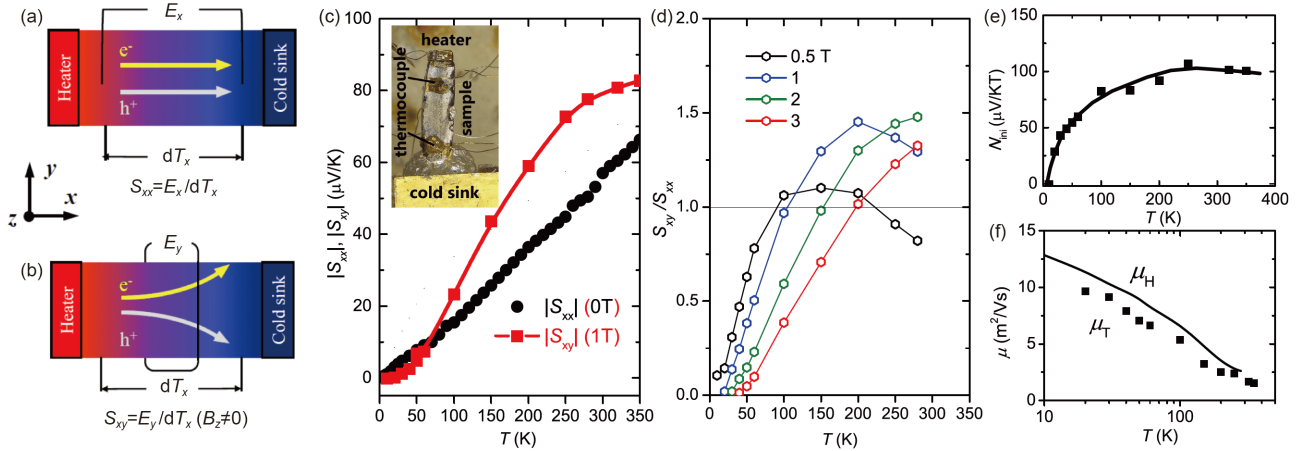


Figure 1 (Color online) Comparison of longitudinal and transverse thermoelectric effects. (a), (b) Schematic illustrations of the Seebeck (S_{xx}) and the Nernst (S_{xy}) effects for a compensated conductor. They measure the longitudinal and transverse thermoelectric voltages E_x and E_y , respectively, over a temperature difference dT_x . For the latter effect, an orthogonal field B_z is usually needed. Note the diminished S_{xx} in (a), as compared to the enhanced S_{xy} in (b) due to electron-hole bipolar conduction. As heat ($\parallel x$) and electric flux ($\parallel y$) are orthogonal in the latter, constraints of the WF law is circumvented when considering thermoelectric application. (c) $S_{xy}(T)$ measured at $B_z = 1$ T, as compared to $S_{xx}(T)$ of Cd_3As_2 . From the quasi-linear behavior of $S_{xx}(T)$, a rough estimate of the Fermi energy $\varepsilon_F = 305$ meV can be obtained by assuming $S_{xx}(T) = (\pi^2/2) \cdot (k_B/e) \cdot (k_B T/\varepsilon_F)$ for simple metals. Inset: the photo image of the sample S1 mounted onto a sample holder. (d) The transverse to longitudinal thermoelectric ratio S_{xy}/S_{xx} at varying field $B_z = 0.5, 1, 2$ and 3 T is shown as a function of T . (e) Initial Nernst coefficient $N_{\text{ini}}(T)$ defined as S_{xy}/B_z ($B_z \rightarrow 0$). (f) Thermoelectric mobility $\mu_T (= N_{\text{ini}}/S_{xx})$ is compared to its electrical analog, i.e., the Hall mobility $\mu_H (= R_H/\rho_{xx})$. Their values are much larger than $1 \text{ m}^2 \text{ V}^{-1} \text{ s}^{-1}$ (i.e., $\omega_c \tau > 1$ at $B_z = 1$ T) below room temperature, indicating that both electric and thermoelectric responses in small fields are predominantly transverse. Data shown in panels (c)-(f) were measured for sample S1, with $x \parallel [110]$ and $z \perp (112)$ plane.

polishing the as-grown samples to typical dimension (3–4) mm \times (1–2) mm \times (0.3–0.5) mm, as shown in Figure 1(c) inset. Note that the field-induced Nernst voltage E_y is geometry (more precisely, the length-to-width ratio) dependent. By convention, we adopt the geometry-normalized Nernst effect $S_{xy} = AE_y/dT_x$, with $A = L_x/L_y$ being the length ratio of thermal and electrical flow [17]. All the thermal-transport measurements were performed within the (112) plane, with magnetic field B_z applied normal to it. The five samples discussed in this work have slightly different Fermi energies, which were estimated from the respective quantum oscillations in electrical resistivity, see Supporting Information.

3 Experimental results

3.1 Transverse versus longitudinal thermoelectricity

As shown in Figure 1(c), for Cd_3As_2 , the magnitude of $S_{xy}(T)$ surpasses that of $S_{xx}(T)$ already in weak magnetic fields, e.g. $B_z = 1$ T, at $T > 100$ K. This is even better demonstrated in Figure 1(d) where the ratio $S_{xy}/S_{xx}(T)$ for $B_z = 0.5, 1, 2$ and 3 T is shown. Furthermore, the initial Nernst coefficient, defined as $N_{\text{ini}} = dS_{xy}/dB_z$ at $B_z \rightarrow 0$, strongly increases with T and reaches $100 \mu\text{V K}^{-1} \text{ T}^{-1}$ at $T \approx 250$ K (Figure 1(e)) before decreasing smoothly. Such $N_{\text{ini}}(T)$ profile has been interpreted for topological semimetal NbP [27] as reflecting the T -dependent competition between electron- and hole-bands, i.e., the bipolar effect. Subsequently, the existence of an enhanced ANE in this material was also emphasized [26],

originating from the shift of the Fermi level ε_F toward the Weyl node upon warming [27]. A larger transverse relative to longitudinal TE response can also be inferred from the so-called thermoelectric mobility $\mu_T = N_{\text{ini}}/S_{xx}$ that is as large as its electrical counterpart, the Hall mobility μ_H ; the latter surmounts $10 \text{ m}^2 \text{ V}^{-1} \text{ s}^{-1}$ at $T = 10$ K, see Figure 1(f). A large value of μ_H pushes the strong field limit ($\mu_H B > 1$) down to below 1 T, where $\omega_c \tau > 1$ is already realized. These properties, in combination with the extremely low thermal conductivity of Cd_3As_2 [28,31], are mainly responsible for the unprecedented magnitude of transverse thermoelectricity in low fields.

Figure 2 compiles the full set of magneto-transport coefficients for sample S1 ($\varepsilon_F = 253$ meV, see Supporting Information) at selected temperatures in panels (a)-(e). In panel (f), we compare the Nernst effect of this sample to the previously reported values in ref. [25]. See Figure S3 for similar results of sample S4 with a higher $\varepsilon_F = 273$ meV. Significantly, both $S_{xx}(B_z)$ and $S_{xy}(B_z)$ (Figure 2(a) and (b)) are sensitive to small fields. At $T > 50$ K, they are substantially enhanced up to a certain value of $B_z \leq 3$ T, then the former quantity tends to saturate and the latter assumes a maximum. In Figure 2(c), $S_{xx}(B_z)$ is compared to $S_{xy}(B_z)$ for $T = 250$ K. There, the value of $S_{xy}(B_z)$ surpasses that of $S_{xx}(B_z)$ at fields as low as $B_z \approx 0.6$ T and by 50% at 2 T, as already indicated by the ratio $S_{xy}/S_{xx}(B_z)$ shown in Figure 1(d). While $S_{xy}(B_z)$ is substantially larger than $S_{xx}(B_z)$ in moderate fields, we note also that the field enhancement to the latter is already sizable and has been reported to cause a marked increase of $z_5 T$ in

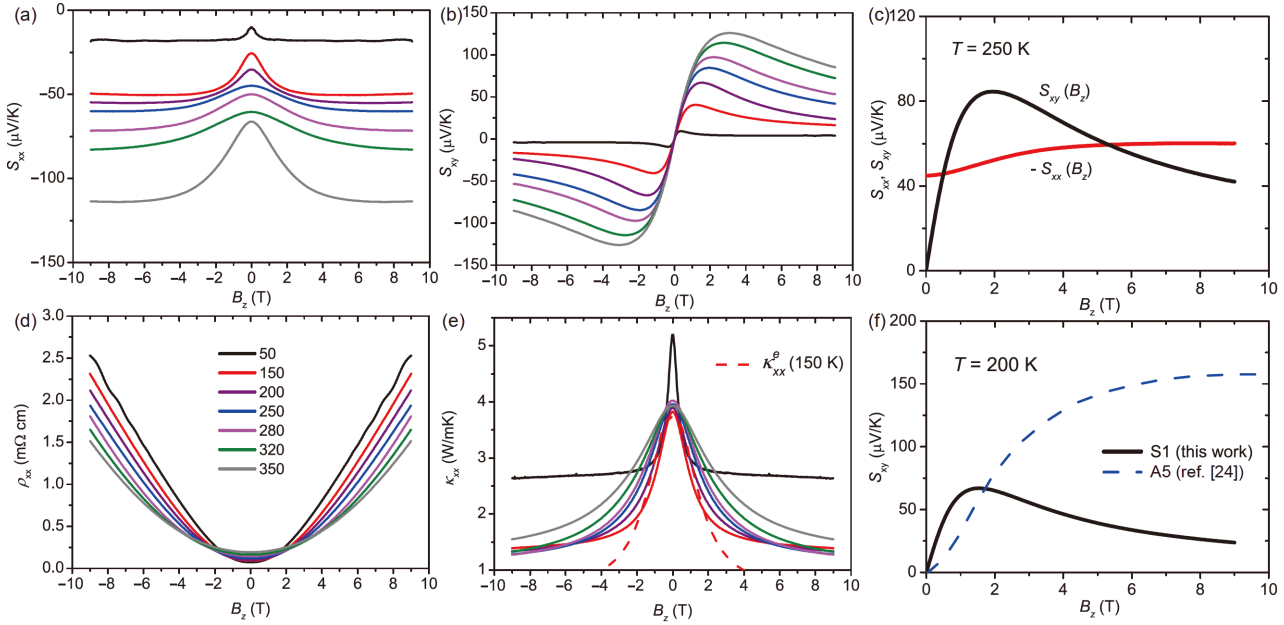


Figure 2 (Color online) Electrical and thermal transport coefficients recorded in perpendicular field scans for sample S1. The Seebeck coefficient $S_{xx}(B_z)$ and Nernst effect $S_{xy}(B_z)$ are shown in (a) and (b), respectively. In (c), $S_{xx}(B_z)$ and $S_{xy}(B_z)$ for $T = 250$ K are compared, with the latter largely exceeding the former between $B_z = 1$ and 4 T. (d) and (e) show electrical resistivity $\rho_{xx}(B_z)$ and thermal conductivity $\kappa_{xx}(B_z)$ at the corresponding temperatures, respectively. Because the electronic contribution $\kappa_{xx}^e(T)$ dominates $\kappa_{xx}(T)$ at $T > 50$ K (see Figure S4), the field enhancement of $\rho_{xx}(B_z)$ and the field reduction of $\kappa_{xx}(B_z)$ are nearly compensated when considering TE application. Namely, $\kappa_{xx}\rho_{xx} \approx L_0T$ in this temperature window. Indeed, as shown in panel (e), the measured $\kappa_{xx}(B_z)$ for $T = 150$ K can be well approached by the calculated $\kappa_{xx}^e (= L_0T/\rho_{xx})$ at $B_z < 2$ T. This means that the denominator of the $z_S T$ expression, $\rho_{xx}\kappa_{xx}$, approximates to a constant and practically, S_{xx} and S_{xy} become the solely free material parameters determining the TE performance. (f) $S_{xy}(B_z)$ measured at $T = 200$ K for sample S1 is compared to that of A5 reported in ref. [25]. The Fermi energy ε_F is 253 and 205 meV for S1 and A5, respectively, see Supporting Information.

Cd_3As_2 [13], as mentioned in the introduction.

As far as TE conversion is concerned, the field-induced increase of $\rho_{xx}(B_z)$ (Figure 2(d)) is almost compensated by the corresponding decrease of $\kappa_{xx}(B_z)$, shown in Figure 2(e), both of which appear in the denominator of $z_S T$ expression. In other words, given that the WF law roughly holds at $T \geq 100$ K for this material, the thermal conductivity measured in this temperature range is predominantly electronic in origin and $\kappa_{xx}\rho_{xx} \approx \kappa_{xx}^e\rho_{xx} = L_0T$. Indeed, as demonstrated in Figure 2(e) for $T = 150$ K, the significant decrease of $\kappa_{xx}(B_z)$ up to $B_z \approx 2$ T can be explained by the estimated $\kappa_{xx}^e(B_z)$ from the WF law (dashed line). For the same reason, the phonon contribution to thermal conductivity, $\kappa_{xx}^{\text{ph}}(T)$, is negligibly small at $T > 100$ K compared to $\kappa_{xx}^e(T)$; see Figure S4. This is due to the intrinsically formed crystallographic vacancies in Cd_3As_2 , which is Cd-deficient of the ideal Cd_4As_2 antiferroite formula [28,31]. Superior electronic transport properties coexisting with negligible phonon thermal conductivity was also observed in other topological semimetals such as WP_2 [32] and ZrTe_5 [33]. This situation is easy to be achieved in a topological semimetal and yields an ideal playground for TE manipulation: here, the figure of merit reduces to $z_S T \approx S_{xx}^2/L_0$ and S_{xx} becomes the only free parameter; a value of $S_{xx} \geq 155$ $\mu\text{V/K}$ would lead to $z_S T \geq 1$. The same argument applies to the Nernst effect as well.

To interpret the large Nernst effect in Cd_3As_2 , comparison

with other semimetals is instructive. Qualitatively similar profiles of both $S_{xx}(B_z)$ and $S_{xy}(B_z)$ as observed in Cd_3As_2 have been found in topological semimetal $\text{Pb}_{1-x}\text{Sn}_x\text{Se}$ with $x = 0.23$, too [34]. There, low-field values of $S_{xy}(B_z)$ are somewhat lower but still sizable. For example, $S_{xy}(B_z = 2 \text{ T}) \approx 50$ $\mu\text{V/K}$ at $T = 250$ K. These values are, however, much smaller than the corresponding values of $S_{xx}(B_z)$. The situation that $S_{xx}(T, B_z) \gg S_{xy}(T, B_z)$ in a large parameter space indicates a much weaker bipolar transport in the aforementioned $\text{Pb}_{1-x}\text{Sn}_x\text{Se}$ compound, qualifying it as a state-of-the-art (longitudinal) TE material [1,2,34]. Consequently, rapid increase of both $S_{xx}(B_z)$ and $S_{xy}(B_z)$ in $\text{Pb}_{1-x}\text{Sn}_x\text{Se}$ ($x = 0.23$) in low fields and at low temperatures ($T < 150$ K) has been successfully approached by a single, high-mobility band [34]. It imposes a competition between longitudinal and transverse differential logarithmic conductivities $D = \partial \ln \sigma_{xx} / \partial \varepsilon$ and $D_H = \partial \ln \sigma_{xy} / \partial \varepsilon$ at the Fermi level. It is this competition that determines the characteristic profiles of $S_{xx}(B_z)$ and $S_{xy}(B_z)$. By employing the experimentally obtained conductivity matrix elements $\sigma_{xx}(B_z)$ and $\sigma_{xy}(B_z)$, we can fit the measured $S_{xx}(B_z)$ and $S_{xy}(B_z)$ for Cd_3As_2 independently. However, the obtained values of $D_H - D$ from the two fittings are already different at $T = 50$ K and the discrepancy further increases with T up to room temperature; see Figure S5. Similar behavior has been discussed as originating from the increasing electron-hole bipolar effect beyond the one-band hypothesis

[34]. This inference applies to Cd_3As_2 as well, being consistent to the inference made from the $N_{\text{ini}}(T)$ profile (Figure 1(e)). Further evidence of bipolar transport in Cd_3As_2 comes from the non-linear $\rho_{xy}(B_z)$ behaviors that indicate a dominating electron band and a hole band that increasingly compensates upon warming; see Figure S6.

3.2 Large transverse thermoelectric figure of merit

In analogy to $z_S T$ that is defined from S_{xx} , its transverse counterpart can be defined from S_{xy} [16],

$$z_N T = T \frac{S_{xy}^2}{\kappa_{xx} \rho_{yy}}, \quad (1)$$

where, κ_{xx} and ρ_{yy} take the values measured along x and y directions, respectively. This definition can be easily rationalized for Nernst configuration, where the induced electrical current ($\parallel y$) is orthogonal to the driving thermal current ($\parallel x$), see Figures 1(b), 3(a) and ref. [16]. In all our samples of Cd_3As_2 , ρ is actually rather isotropic at least within the focused (112) plane (Figure S7). We therefore use the simultaneously measured ρ_{xx} , rather than the separately measured ρ_{yy} , to compute $z_N T$ in order to reduce systematic errors. As shown in Figure 3(b), superiority of the transverse over the longitudinal TE effect in Cd_3As_2 is immediately apparent: $z_N T(B_z)$ exhibits a maximum which, at $T > 150$ K, is not only higher but also occurs in a lower field (B_z^{max}) compared to the maximum in $z_S T(B_z)$. These maximum zT values, denoted as $z_N T^{\text{max}}$ and $z_S T^{\text{max}}$, respectively, are shown as a function of T in Figure 3(c). There, $z_N T^{\text{max}}$ is increasingly enhanced with temperature over its longitudinal counterpart by, e.g., approximately 50% at $T = 350$ K. After being normalized by their corresponding fields as $z_N T^{\text{max}}/B_z^{\text{max}}$, the contrast between the two configurations becomes even more striking, see Figure 3(d). Above $T = 150$ K, the maximum zT value per Tesla of the transverse TE configuration exceeds its longitudinal counterpart by about a factor of two in a wide temperature range.

Despite its marked increase at low fields, the value of $z_N T$ is still inadequate for practical TE applications. A key parameter yet to be optimized is the Fermi energy ϵ_F , which determines the magnitude of not only the one-band and bipolar diffusion contributions to S_{xy} [18,35], but also the ANE [24-27]. A reduction of ϵ_F is expected to enhance all the relevant contributions to S_{xy} in a Dirac semimetal. To clarify this point, we have derived the values of ϵ_F for all the employed samples from the experimentally observed quantum oscillations in $\rho_{xx}(B_z)$, see Figure S8. Note that, within the charge-neutrality condition, ϵ_F is measured with respect to the energy of minimal electronic density of states, i.e., the energy of the Dirac node. As shown in Figure 4, ϵ_F spans the range of roughly 250-290 meV from sample S1 to S5, in agreement with previous report [29]. Most importantly and

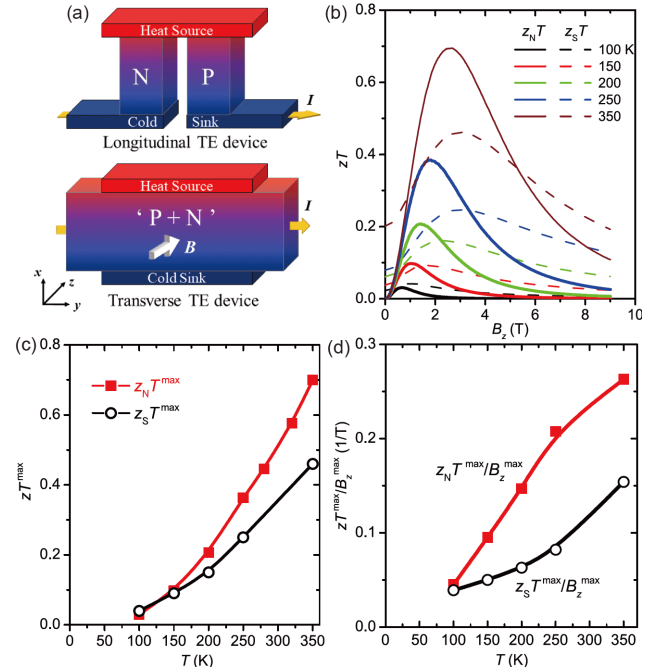


Figure 3 (Color online) Enhanced transverse thermoelectricity in Cd_3As_2 . (a) Schematics of longitudinal (upper) and transverse (lower) TE devices. While the former needs both p - and n -type materials, the latter uses only one material with, however, inherent contributions from both types of charge carrier through bipolar transport. (b) $z_N T(B_z)$ in comparison to $z_S T(B_z)$ at selected temperatures for sample S1. (c) $z_N T^{\text{max}}$ and $z_S T^{\text{max}}$, i.e., the maximum values of $z_N T(B_z)$ and $z_S T(B_z)$ observed at certain field B_z^{max} , are shown as a function of T . (d) $z_N T^{\text{max}}$ is normalized by the corresponding field B_z^{max} for both longitudinal and transverse configurations, where the latter amounts to more than two times the former over a large temperature range above 100 K.

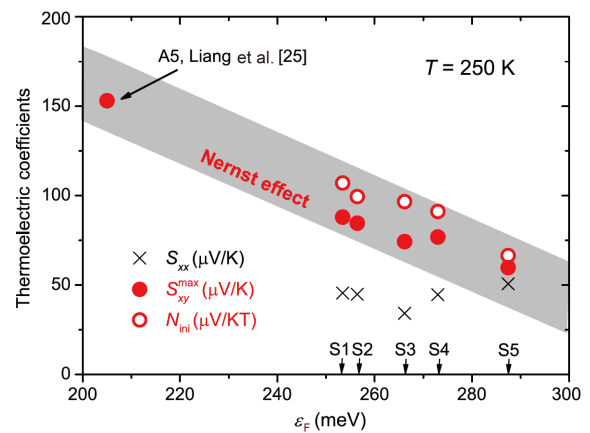


Figure 4 (Color online) Longitudinal and transverse thermoelectric coefficients as a function of ϵ_F at $T = 250$ K. S_{xy}^{max} denotes the maximum values of $S_{xy}(B_z)$, see Figures 2(b) and S3(b), N_{ini} the initial Nernst coefficient (cf. Figure 1(e)). Both quantities increase monotonically with lowering ϵ_F , owing to the simultaneously enhanced single-band and bipolar diffusion contributions. Given the existence of ANE arising from Berry curvature in Cd_3As_2 , it will also increase with lowering ϵ_F [24-27]. The data point for sample A5 at $\epsilon_F = 205$ meV (reproduced from ref. [25]; see Figure 2(f), too) was measured at $T = 200$ K; it would presumably lead to a significant $z_N T$ close to unity, see maintext. By contrast, the Seebeck coefficient S_{xx} at zero field reveals no significant ϵ_F dependence. This can be easily understood by considering the opposite trend of single-band and bipolar effect in longitudinal thermoelectric effect as a function of ϵ_F .

instructively, both S_{xy}^{\max} and N_{ini} , which characterize the magnitude of the transverse Nernst effect, increase monotonically with lowering ε_F . A simple extrapolation indicates that S_{xy}^{\max} would be greater than 155 $\mu\text{V/K}$ if $\varepsilon_F < 200$ meV. Unfortunately, our sample syntheses could not yield reliable samples with $\varepsilon_F < 250$ meV. One batch (A5) reported in ref. [25], with $S_{xy}^{\max} \approx 150$ $\mu\text{V/K}$ at $B_z = 5$ T, is reproduced in Figure 2(f); the Fermi energy of this sample is estimated to be $\varepsilon_F \approx 205$ meV (see Supporting Information), which indeed meets our expectation for larger S_{xy} , cf. Figure 4. Given the dominating κ_{xx}^e in this temperature range, this very sample should exhibit a maximum $z_N T$ of order unity at $T = 200$ K. This simple relation between the Nernst effect and ε_F reflects the aforementioned monotonic enhancement of all quantities contributing to S_{xy} upon decreasing ε_F . By contrast, for the five samples investigated in this work we could not find any significant variation of the zero-field values of S_{xx} . As discussed in the introduction, this is most likely due to a competition between bipolar and single-band Seebeck effects, where the former diminishes and the latter enhances the value of S_{xx} upon lowering ε_F [17].

4 Discussion

Our observations of large $S_{xy}(T, B_z)$ values over those of $S_{xx}(T, B_z)$ in a wide parameter space is not specific to Cd_3As_2 , but is generally expected in topological semimetals. An extraordinarily large value of $S_{xy}(T = 109 \text{ K}; B_z = 9 \text{ T}) \approx 800$ $\mu\text{V/K}$ was recently observed in NbP, and found to be two orders of magnitude larger than the corresponding value of S_{xx} [27]. This is not surprising because in NbP $\varepsilon_F = 8.2$ meV is much closer to the Weyl node. This leads to symmetric electron-hole excitations that are essential for a strong bipolar contribution to S_{xy} , as well as an enhanced Berry curvature strength [24,26] that gives rise to large values of ANE. Unfortunately, the thermal conductivity of NbP ($\kappa \approx 250 \text{ W K}^{-1} \text{ m}^{-1}$ at $T = 300$ K) is much too large to obtain a sizable $z_N T$ value [20,36]. In WP_2 , too, a large Nernst was observed, e.g., $S_{xy}(T = 3.66 \text{ K}, B_z = 5 \text{ T}) \approx 1$ mV/K, albeit at much lower temperatures [37]. As has been discussed, due to the generically high mobility of all the pertinent Dirac/Weyl semimetals, the strong-field limit with $\omega_c \tau > 1$ can be easily accessed by a field as low as 1 T. There, a larger value of S_{xy} over S_{xx} is anticipated, resembling the case of dominating transverse electrical conductivity with $\sigma_{xy} > \sigma_{xx}$, see Figure 1(d) and refs. [27,37]. This is a field accessible even by commercial permanent magnet like $\text{Nd}_2\text{Fe}_{14}\text{B}$. Recently, Nernst effect in the absence of external field has been observed in a magnetic topological semimetal [38]. This effect can in principle remove the external magnetic field that has been so far considered necessary for transverse TE application, and certainly deserves more attention in future.

As already demonstrated for Cd_3As_2 [25], a steplike increase of $S_{xy}(B_z)$ in low fields arising from enhanced Berry curvature and characterizing the ANE is a significant addition to the conventional (diffusive) Nernst effect. This occurs if the Fermi level is sufficiently reduced towards the Dirac/Weyl node [23-26], which may be achieved by a well-controlled sample synthesis. Such a situation appears to be realized for the case of sample A5 in ref. [25]; its maximum value of $S_{xy}(B_z)$ is reproduced in Figure 4. A direct identification of a steplike ANE for our samples seems unlikely, see Figures 2(b) and S3(b). However, such a contribution is presumably involved in our samples, too, though being expected to be smaller given their higher ε_F . Whether in future one can experimentally sort out the evolution of the ANE with ε_F appears to be instructive for the improvement of S_{xy} . The largely unexplored ANE in this compound, together with the enhanced diffusive and bipolar contribution to S_{xy} , promises a large room for further optimization of $z_N T$. This is believed to be achievable simply by tuning the Fermi energy, as shown in Figure 4.

Apart from their fundamental advantages discussed above, transverse TE devices also have remarkable merits due to their unique configuration geometry. (i) The TE conversion output of such devices scales with the sample size along y relative to x , which allows for various possibilities of shape engineering in order to maximize conversion efficiency [16]; (ii) both electrons and holes of a single material are already involved in the Nernst effect, leaving out the traditional idea of employing both n and p -type materials in one TE device, see Figure 3(a); (iii) separation of electrical and heat flows into two orthogonal directions removes the fundamental constraint of the WF law; utilization of anisotropic transport becomes possible through, e.g., combining low κ_{xx} and low ρ_{yy} in one material.

5 Conclusion

In summary, we have observed sizable values of transverse thermoelectric figure of merit (e.g. $z_N T \approx 0.5$ at $T = 300$ K) in the topological Dirac semimetal Cd_3As_2 . The large values of $z_N T$ result primarily from the enhanced Nernst effect. The latter effect benefits significantly from the charge compensation of pertinent electrons and holes and their high mobilities that are inherent to many topological semimetals. Further optimization of the Nernst effect can be highly expected by tuning the Fermi level towards the Dirac/Weyl node; this will cause not only an enhanced bipolar transport, but also an anomalous Nernst effect due to the enhanced Berry curvature. Importantly, the fundamental constraints applying to the Seebeck-effect-based thermoelectric devices, i.e., the charge compensation and the Wiedemann-Franz law, are fully removed in the Nernst configuration. In view all

these topologically trivial and nontrivial advantages of transverse thermoelectricity, further investigations of other topological semimetals along the same line are badly called for.

This work was supported by the Ministry of Science and Technology of China (Grant Nos. 2017YFA0303100, and 2015CB921303), the National Natural Science Foundation of China (Grant Nos. 11774404, and 11474332), and the Chinese Academy of Sciences through the Strategic Priority Research Program (Grant No. XDB07020200).

Supporting Information

The supporting information is available online at phys.scichina.com and link.springer.com. The supporting materials are published as submitted, without typesetting or editing.

- 1 G. J. Snyder, and E. S. Toberer, *Nat. Mater* **7**, 105 (2006).
- 2 J. He, and T. M. Tritt, *Science* **357**, eaak9997 (2017).
- 3 G. A. Slack, *CRC Handbook of Thermoelectrics*, D. M. Rowe, ed (CRC Press, Boca Raton, 1995).
- 4 L. MÜchler, F. Casper, B. Yan, S. Chadov, and C. Felser, *Phys. Status. Solidi. RRL* **7**, 91 (2013), arXiv: 1209.6097.
- 5 K. Pal, S. Anand, and U. V. Waghmare, *J. Mater. Chem. C* **3**, 12130 (2015).
- 6 H. Shi, D. Parker, M. H. Du, and D. J. Singh, *Phys. Rev. Appl.* **3**, 014004 (2015), arXiv: 1412.5407.
- 7 Devender, P. Gehring, A. Gaul, A. Hoyer, K. Vaklinova, R. J. Mehta, M. Burghard, T. Borca-Tasciuc, D. J. Singh, K. Kern, and G. Ramanath, *Adv. Mater.* **28**, 6436 (2016).
- 8 R. Lundgren, P. Laurell, and G. A. Fiete, *Phys. Rev. B* **90**, 165115 (2014), arXiv: 1407.1435.
- 9 Y. Xu, Z. Gan, and S. C. Zhang, *Phys. Rev. Lett.* **112**, 226801 (2014), arXiv: 1403.3137.
- 10 R. Takahashi, and S. Murakami, *Semicond. Sci. Technol.* **27**, 124005 (2012).
- 11 S. Wang, B. C. Lin, A. Q. Wang, D. P. Yu, and Z. M. Liao, *Adv. Phys.-X* **2**, 518 (2017).
- 12 N. P. Armitage, E. J. Mele, and A. Vishwanath, *Rev. Mod. Phys.* **90**, 015001 (2018), arXiv: 1705.01111.
- 13 H. Wang, X. Luo, W. Chen, N. Wang, B. Lei, F. Meng, C. Shang, L. Ma, T. Wu, X. Dai, Z. Wang, and X. Chen, *Sci. Bull.* **63**, 411 (2018).
- 14 B. Skinner, and L. Fu, *Sci. Adv.* **4**, eaat2621 (2018), arXiv: 1706.06117.
- 15 W. M. Yim, and A. Amith, *Solid-State Electron.* **15**, 1141 (1972).
- 16 H. J. Goldsmid, *Br. J. Appl. Phys.* **14**, 271 (1963).
- 17 H. J. Goldsmid, *Introduction to Thermoelectricity* (Springer, Heidelberg, 2009).
- 18 K. Behnia, M. A. Méasson, and Y. Kopelevich, *Phys. Rev. Lett.* **98**, 076603 (2007).
- 19 A. Pourret, K. Behnia, D. Kikuchi, Y. Aoki, H. Sugawara, and H. Sato, *Phys. Rev. Lett.* **96**, 176402 (2006).
- 20 C. Fu, S. N. Guin, S. J. Watzman, G. Li, E. Liu, N. Kumar, V. Süß, W. Schnelle, G. Auffermann, C. Shekhar, Y. Sun, J. Gooth, and C. Felser, *Energy Environ. Sci.* **11**, 2813 (2018).
- 21 D. Xiao, Y. Yao, Z. Fang, and Q. Niu, *Phys. Rev. Lett.* **97**, 026603 (2006).
- 22 G. Sharma, P. Goswami, and S. Tewari, *Phys. Rev. B* **93**, 035116 (2016), arXiv: 1507.05606.
- 23 J. Noky, J. Gooth, C. Felser, and Y. Sun, *Phys. Rev. B* **98**, 241106 (R) (2018), arXiv: 1807.07843.
- 24 F. Caglieris, C. Wuttke, S. Sykora, V. Süß, C. Shekhar, C. Felser, B. Büchner, and C. Hess, *Phys. Rev. B* **98**, 201107(R) (2018).
- 25 T. Liang, J. Lin, Q. Gibson, T. Gao, M. Hirschberger, M. Liu, R. J. Cava, and N. P. Ong, *Phys. Rev. Lett.* **118**, 136601 (2017), arXiv: 1610.02459.
- 26 G. Sharma, C. Moore, S. Saha, and S. Tewari, *Phys. Rev. B* **96**, 195119 (2017), arXiv: 1605.00299.
- 27 S. J. Watzman, T. M. McCormick, C. Shekhar, S. C. Wu, Y. Sun, A. Prakash, C. Felser, N. Trivedi, and J. P. Heremans, *Phys. Rev. B* **97**, 161404 (R) (2018), arXiv: 1703.04700.
- 28 C. Zhang, T. Zhou, S. Liang, J. Cao, X. Yuan, Y. Liu, Y. Shen, Q. Wang, J. Zhao, Z. Yang, and F. Xiu, *Chin. Phys. B* **25**, 017202 (2016).
- 29 L. P. He, X. C. Hong, J. K. Dong, J. Pan, Z. Zhang, J. Zhang, and S. Y. Li, *Phys. Rev. Lett.* **113**, 246402 (2014), arXiv: 1404.2557.
- 30 T. Liang, Q. Gibson, M. N. Ali, M. Liu, R. J. Cava, and N. P. Ong, *Nat. Mater.* **14**, 280 (2015), arXiv: 1404.7794.
- 31 M. N. Ali, Q. Gibson, S. Jeon, B. B. Zhou, A. Yazdani, and R. J. Cava, *Inorg. Chem.* **53**, 4062 (2014).
- 32 J. Gooth, F. Menges, N. Kumar, V. Süß, C. Shekhar, Y. Sun, U. Drechsler, R. Zierold, C. Felser, and B. Gotsmann, *Nat. Commun.* **9**, 4093 (2018).
- 33 J. Zhu, T. Feng, S. Mills, P. Wang, X. Wu, L. Zhang, S. T. Pantelides, X. Du, and X. Wang, *ACS Appl. Mater. Interfaces* **10**, 40740 (2018).
- 34 T. Liang, Q. Gibson, J. Xiong, M. Hirschberger, S. P. Koduvayur, R. J. Cava, and N. P. Ong, *Nat. Commun.* **4**, 2696 (2013).
- 35 K. Behnia, and H. Aubin, *Rep. Prog. Phys.* **79**, 046502 (2016), arXiv: 1601.06647.
- 36 U. Stockert, R. D. Dos Reis, M. O. Ajeesh, S. J. Watzman, M. Schmidt, C. Shekhar, J. P. Heremans, C. Felser, M. Baenitz, and M. Nicklas, *J. Phys.-Condens. Matter* **29**, 325701 (2017), arXiv: 1704.02241.
- 37 Z. Zhu, X. Lin, J. Liu, B. Fauqué, Q. Tao, C. Yang, Y. Shi, and K. Behnia, *Phys. Rev. Lett.* **114**, 176601 (2015), arXiv: 1502.07797.
- 38 S. N. Guin, P. Vir, Y. Zhang, N. Kumar, S. J. Watzman, C. Fu, E. Liu, K. Manna, W. Schnelle, J. Gooth, C. Shekhar, Y. Sun, and C. Felser, *Adv. Mater.* **31**, 1806622 (2019).